Available online at www.sciencedirect.com
ScienceDirect
Journal of Solid State Chemistry 179 (2006) 3849–3859
JOURNAL OF SOLID STATE CHEMISTRY
www.elsevier.com/locate/jssc

Disordered commensurate structure of the 2212-related phase $Fe_2(Bi_{0.69}Sr_{2.31})Fe_2O_{9.5\pm1/2\delta}$ and structural mechanism

Dominique Grebille*, Christophe Lepoittevin, Sylvie Malo, Oliver Pérez, N. Nguyen, Maryvonne Hervieu

Laboratoire CRISMAT (UMR CNRS 6508), ENSICAEN, Bd du Maréchal Juin, 14050 Caen Cedex, France

Received 26 May 2006; received in revised form 1 August 2006; accepted 5 August 2006
Available online 1 September 2006

Abstract

The structure of the $Fe_2(Bi_{0.69}Sr_{2.31})Fe_2O_{9.5-1/2\delta}$ has been carried out by single crystal X-ray diffraction. Its structure can be considered as commensurately modulated with a basic structure of *Fmmm* symmetry and with a modulation vector $\vec{q} = \alpha\vec{a}^* + \gamma\vec{c}^*$ whose α and γ values are, respectively, equal to 1/3 and 1. The ferrite is described as a three-fold superstructure with $a \approx 3\,a_p\sqrt{2}$, $b \approx a_p\sqrt{2}$ and $c \approx 26$ Å (space group *Bbmb*). It is described using a disorder model in agreement with diffuse scattering observations. The structure is built up from the intergrowth sequence between $[(Bi, Sr)Fe_2O_{3.5\pm1/2\delta}]_\infty$ complex layers, related to the rock salt (RS)-type blocks, and double perovskite layers. Large analogies are found between the present structure and the so-called 2212 modulated structures related to the high T_c superconductor copper oxides or to the corresponding Fe or Co oxides; they are discussed here. A statistical disorder characterizes the $[Fe_2O_{2.5\pm1/2\delta}]_\infty$ double layer. Taking advantage of similar structural arrangements in related oxide compounds, a structural model is proposed. A description of this double layer is then given in terms of sequence of polyhedra (tetragonal pyramids, mono-caped tetrahedra and trigonal bi-pyramids), in comparison with other related modulated structures with different periodicities. The powder sample exhibits a statistical distribution of α around an average value of 0.35; the oxygen non-stoichiometry appears as the driving force for the α value, i.e. for the modulation, commensurate or incommensurate. The Mössbauer study has been performed and interpreted on the basis of the refined structure.

Keywords: Ferrite; Modulated structure; Superstructure; Disorder

1. Introduction

The strontium ferrite and cobalt-doped compounds $Sr_4(Fe_{6-x}Co_x)O_{13\pm\delta}$ are interesting materials due to their mixed-conducting behaviour and their potential applications to high-temperature electrochemical processes, ceramic membranes for oxygen separation and partial oxidation of hydrocarbons [1–9], on the one hand, and to their stability and high values of thermoelectric power [10] by calcium for strontium doping, on the other hand. One of the keys of these properties is the wide range of oxygen stoichiometry, $O_{13\pm\delta}$, easily accommodated in the framework. The first papers devoted to the structure of these materials [11–15] described the average structures, outlining their high complexity. In fact, the $Sr_4Fe_6O_{13\pm\delta}$, phases are modulated structures [16–18], the amplitude of the modulation vector being directly correlated to the oxygen content [17]. High-resolution electron microscopy (HREM) images [11–13] allowed first structural models to be proposed for explaining the incommensurate character of the modulated phases. However, these images cannot provide unambiguous answer to one important issue about the exact nature of the iron polyhedra.

The incommensurate modulated structure of $Sr_4Fe_6O_{13-\delta}$ was refined in 4D formalism, from single crystal X-ray diffraction data [19]. The description of the structure from the intergrowth along $\vec{c}$ of one perovskite slice $[SrFeO_3]_\infty$ and one complex $[SrFe_2O_{3.5\pm\delta/2}]_\infty$ slice, related to a rock salt (RS)-type block, suggests that this compound belongs to the large so-called "2201" family, code previously adopted for describing the superconducting cuprates and derivatives.

*Corresponding author. Fax: +33 2 31 95 16 00.
E-mail address: dominique.grebille@ensicaen.fr (D. Grebille).

0022-4596/$ - see front matter © 2006 Elsevier Inc. All rights reserved.
doi:10.1016/j.jssc.2006.08.015

The $[SrFe_2O_{3.5\pm\delta/2}]_\infty$ slice is built up from two [SrO] layers sandwiching one complex $[Fe_2O_{2.5\pm1/2\delta}]_\infty$ double layer. In the latter, three types of edge sharing iron (FeO_5) polyhedra running along $\vec{a}$, have been evidenced, namely, tetragonal pyramids (TPs), trigonal bipyramids (TBPs) and mono-caped tetrahedra (MTs). This accurate analysis characterized the different types of blocks associated to the existence of the original ([TBP↑][TBP↓]) units and the distortion they impose to the different adjacent polyhedra associated to oxygen non-stoichiometry.

Another original compound, $Bi_{4/3}Sr_{14/3}Fe_8O_{19\pm\delta}$ [20], has been isolated, built up from the intergrowth of one double perovskite slice $[(Bi,Sr)_2Fe_2O_6]_\infty$ and one complex $[(Bi,Sr)Fe_2O_{3.5\pm\delta/2}]_\infty$ slice, showing that the latter is a stable structural unit and outlining the relationships with the large family of the 2201s and 2212s [21]. The electron diffraction (ED) study revealed an orthorhombic sub-cell with $a \approx b \approx a_p\sqrt{2}$ and $c \approx 26$ Å with reflection conditions corresponding to a F lattice (*Fmmm*, *Fmm*2 and *F*222). However, a super-cell, corresponding to a modulation along the $\vec{a}$ axis, has been evidenced with a two components modulation vector $\vec{q} = \alpha\vec{a}^* + \gamma\vec{c}^*$ whose α and γ values are respectively equal to 1/3 and 1. Because of the commensurability of this modulation vector, the ferrite is described in a 3D lattice with $a \approx 3\,a_p\sqrt{2}$, $b \approx a_p\sqrt{2}$ and $c \approx 26$ Å, and the structure was refined using single crystal X-ray diffraction data.

The present paper deals with the accurate determination of the iron polyhedra in the $[SrFe_2O_{3.5\pm\delta/2}]_\infty$ slices and the nature of the different blocks sequence along $\vec{a}$. The large analogies found with the so-called 2212 structures related to the high T_c superconductor copper oxides or to the corresponding Fe or Co oxides are discussed. A powder sample has been also prepared for Mössbauer and electron microscopy studies in order to collect accurate information, especially at the level of the iron environment, and to perform a good correlation thanks to the fitted spectrum and calculated images on the basis of the refined structure.

2. Experimental

The powder sample was prepared as previously described [20], starting from Bi_2O_3, Fe_2O_3 and SrO. The different oxides, weighed in the stoichiometric ratio were ground in an agate mortar and pressed into bars in a glove box, then sealed in a silica tube. They were heated at 1100 °C for 48 h, with a heating rate of 2 °C/min and slow cooled at the same rate. The EDS analyses confirmed the adequate Bi/Sr/Fe ratio and the powder diffraction X-ray pattern confirmed that the sample is single phased.

The iron oxidation state was determined using a cerimetric titration which allows to calculate the oxygen stoichiometry. The sample (≈25 mg) is dissolved in 50 mL of HCl (1 N) solution containing $FeCl_2 \cdot 4H_2O$ (1 M). The solution is titrated with $Ce(SO_4)_2$ solution (0.015 M).

Table 1
Crystal data and refinement results

Refined chemical formula	$Bi_{0.69}Sr_{2.31}Fe_4O_{9.33}$
Cell parameters	$a = 16.592(10)$ Å
	$b = 5.555(1)$ Å
	$c = 27.101(7)$ Å
Space group	*Bbmb*
Z	2
Absorption correction	Empirical (SADABS Software)
Internal R value (%) before/after absorption correction	11.4/5.56
Redundancy	8.64
Weighting scheme	$1/\sigma^2(I)$
Unique reflections	1210
Refinement parameters R/R_w	101
Global (1210)	4.85/2.85
Main reflections ($h = 3n$) (566)	3.29/2.47
Satellite reflections ($h \neq 3n$) (644)	8.38/5.60
$\Delta\rho_{min}/\Delta\rho_{max}$	$-6.0/6.6$ e Å^{-3}

Single crystals were prepared starting from a mixture of Bi_2O_3, Fe_2O_3 and SrO in a glove box. The powders were weighed according to the stoichiometric ratio, ground in an agate mortar and introduced in an alumina crucible before being sealed in a silica tube. Then, the mixture was heated following the thermal cycle: heating at 1200 °C for 48 h, with a heating rate of 3 °C/min, slow cooled to 1000 °C at a rate of 5 °C/h and finally cooled to room temperature.

The single crystal X-ray diffraction study was performed at room temperature using Mo$K\alpha$ radiation with a Bruker Kappa CCD diffractometer. A first cell was determined using reflections with $\theta < 30°$ and is compatible with the orthorhombic system: $a = 16.592(10)$ Å, $b = 5.555(1)$ Å, $c = 27.101(7)$ Å. Data collection was performed using $\phi-\omega$ scans with $0 < \theta < 45°$, with steps of 0.3°/frame and a sample detector distance of 34 mm. Data reduction and integration was performed using the EVALCCD software [22]. Absorption corrections were applied using the SADABS program [23]. Crystal data are summarized in Table 1. Structure refinement was performed using the JANA2000 software package [24].

The ED study was carried out with a JEOL 200CX electron microscope and the high resolution imaging with a TOPCON 002B (200 kV, Cs = 0.4 mm), equipped with energy dispersive spectroscopy (EDS) analysers.

The ^{57}Fe powder Mössbauer resonance spectrum was performed at 80 K with a transmission geometry by use of a constant acceleration spectrometer and a γ-ray source from ^{57}Co embedded in a rhodium matrix. The velocity scale was calibrated with an α-Fe foil at room temperature. The spectrum was fitted with Lorenzian lines by the MOSFIT program. The isomer shift was referred to metallic α-Fe at 293 K.

3. Diffraction and symmetry

Plots of reciprocal lattice planes were calculated from the data collection. Intense main reflections can be clearly

distinguished from weak satellite reflections (Figs. 1 and 2). An average cell can be defined with $\mathbf{a_0} = \mathbf{a}/3$, $\mathbf{b_0} = \mathbf{b}$ and $\mathbf{c_0} = \mathbf{c}$ and, considering the observed reflection conditions, is compatible with the *Fmmm* space group. Satellite reflections can be indexed using the modulation vector $\mathbf{q} = \alpha\mathbf{a_0}^* + \mathbf{c}^*$, with $\alpha = 1/3$. The structure can be interpreted as a commensurate modulated structure. These results are in agreement with the previous ED study [20].

Using the 4D super-space formalism for modulated structures [25,26], the diffraction pattern can be described with the super-space group $Fmmm(\alpha 01)0\,0\,s$, compatible

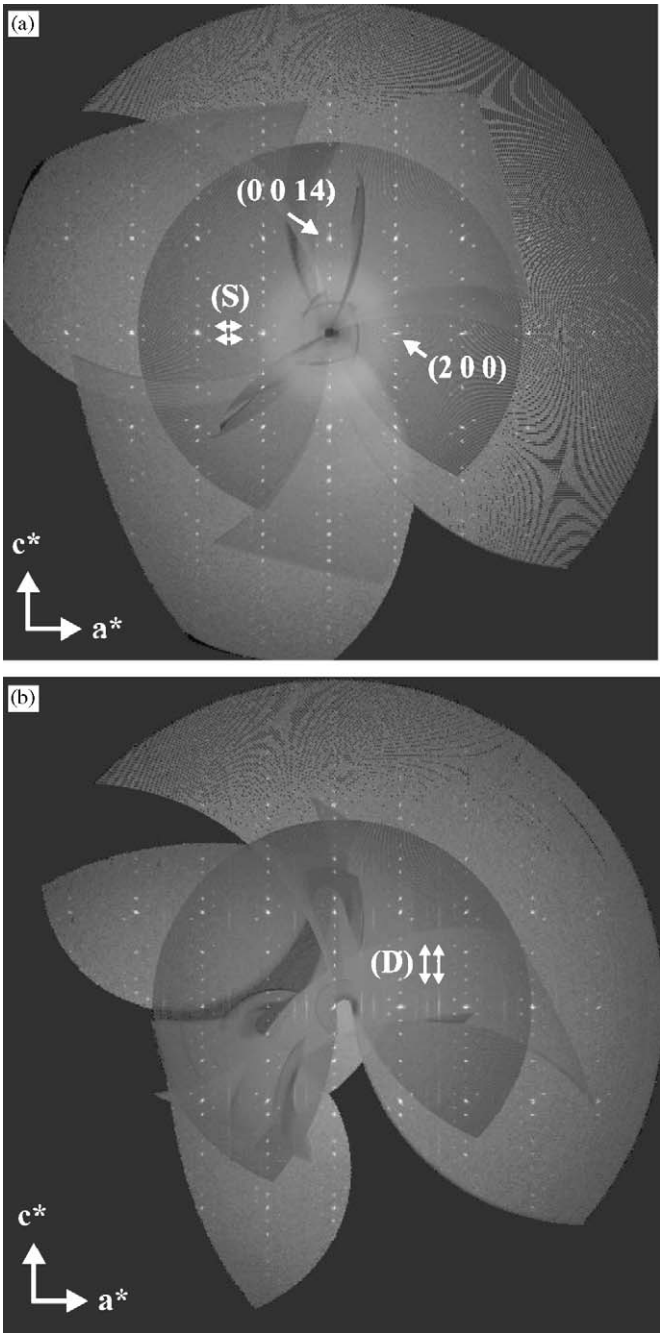

Fig. 1. Synthetic precession images of the (*h*0*l*) (a) and (*h*2*l*) planes of the diffraction pattern. Main reflections are indexed in the average *Fmmm* cell. S show first order satellites, and D, diffuse scattering lines.

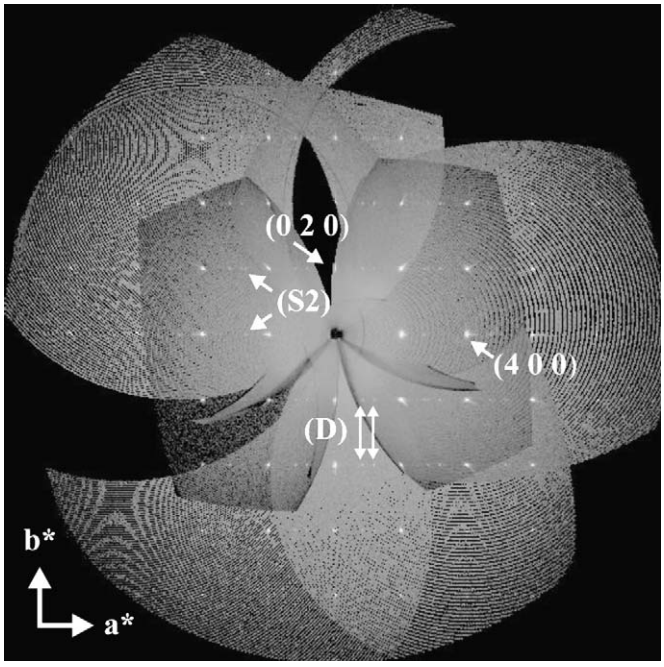

Fig. 2. Synthetic precession images of the (*hk*0) plane of the diffraction pattern. Main reflections are indexed in the average *Fmmm* cell. S2 show second-order satellites, and D, the trace in this plane of the diffuse scattering lines.

with the usual *F* centring conditions and with the reflection condition : (*hk*0*m*) $m = 2n$. According to the low rational value of α, the structure was described and refined in the triple super-cell $\mathbf{a} = 3\mathbf{a_0}$. Three possible symmetries for the superstructure are compatible with the previous super-space group, according to the choice of the *t* section [25]. The $t = 0$ section, corresponding to the *Bbmb* group compatible with both the present observed reflection conditions and ED characterization (present work and [20]), is chosen for the refinement.

Additional weak diffuse scattering lines along **c*** could also be observed in the precession images, with increasing intensities for higher values of *k* (D in Fig. 1b), and for $l \approx 12n$. They are located along $((h_0 \pm 5/6)a^*, k_0 b^*, z)$, with h_0 and k_0 corresponding to high intensity main reflections of the *F* average lattice. They correspond to apparent supplementary satellite reflections in the (*hk*0) section of the diffraction pattern (D in Fig. 2). They can be interpreted by the presence of a structural disorder along the stacking direction **c***, but with an ordered modulated structural scheme along **a***. Similar diffuse scattering phenomena could also be observed in related structures [19]. Their presence will be discussed later.

4. Structure refinement

A preliminary model was used based on the first structural hypothesis concerning the $Bi_{4/3}Sr_{14/3}Fe_8O_{19\pm\delta}$ phase. It consists in the stacking along **c** of double perovskite layers [$(Sr, Bi)_4Fe_4O_{12}$] (slab A) and complex [$(Sr, Bi)_2Fe_4O_{7-\delta}$] layers (slab B). Three iron atomic sites

Fe_A in 8*l* positions, four equatorial oxygen sites, O_e in 8*h* and 16*m* positions, five apical oxygen sites O_a, one in 4*e* positions and the others in 8*l* positions are necessary to build the FeO_6 octahedra of the perovskite layer. Sr atoms occupy the same types of sites than the previous oxygen atoms. Refinement of the occupancy of these Sr sites proved that the two sites Sr2(1) and Sr2(2) between the two FeO_6 octahedra of the double perovskite slab are only occupied with Sr, whereas the other sites Sr1, on each side of the layer, are partially occupied with around 35% of Bi. This mixed site can be considered as a common site to the A and B slabs.

Trying to locate iron positions in the intermediate layer (around $z = 0$ or 0.5), the observed electron density in corresponding Fourier maps (Fig. 3) shows a splitting of the atomic sites on each site of the mirror plane orthogonal to **b**. As a consequence, three split iron atomic sites Fe_B in general 16*m* positions were introduced with a half-occupation, allowing a significant decrease of the agreement factor. Then, oxygen atomic sites were defined according to Fourier difference maps, also in three split disordered sites 16*m* O_B, and one supplementary oxygen atom O_{Bs} in 4*a* positions.

The corresponding calculated formula is $Bi_{1.39}Sr_{4.61}Fe_8O_{18.67}$, very closed to the estimated chemical formula by EDS and by chemical analyses. Assuming the valences +3, +2 and −2 for Bi, Sr and O, respectively, this is compatible with an average valence +3 for Fe.

Anisotropic atomic displacement parameters were refined for non-disordered cationic sites, and isotropic ones for the others. The final refinement converged to a global good agreement $R_w = 0.0285$ for 1210 averaged observed reflections and 101 refinement parameters. Partial agreement factors were calculated concerning specifically main and satellite reflections and are given in Table 1. Refined structural parameters are given in Table 2.

One may expect to raise the disorder resulting from the splitting of atomic positions in the [(Bi, Sr)$Fe_2O_{3.5}$] blocks by a lowering of the symmetry in acentric symmetries with the suppression of the m_y mirror plane. Different trials in the two maximal orthorhombic subgroups *Bb*2*b* and *B*222 were performed, with different initial configurations obtained by different choices of the atomic Fe and O positions among all the possible disordered positions, and considering the likely occurrence of a twin in relation with the lost of the mirror plane. For these calculations, a non-averaged data set was used including Friedel pairs. In all cases, the refinement is very instable and characterized by a lot of correlations, and imposes the use of an important damping factor. The final agreement factor is 0.048 for 160 refinement parameters in the *Bb*2*b* space group. For comparison, the refinement in the centrosymmetric *Bbmb* group gives an agreement factor of 0.053 for 101 refinement parameters. One does not observe any significant deviation of the non-split atomic positions. The split ones keep a mixed occupation, with more or less deviations from the half-occupation, but systematically, the twin volume ratio is refined very closed to 0.5, which supports the centric solution. The corresponding observed Fourier maps always show split electron density maxima very similar to Fig. 3. Moreover, the acentric solution gives not positive definite ADP harmonic parameters for several

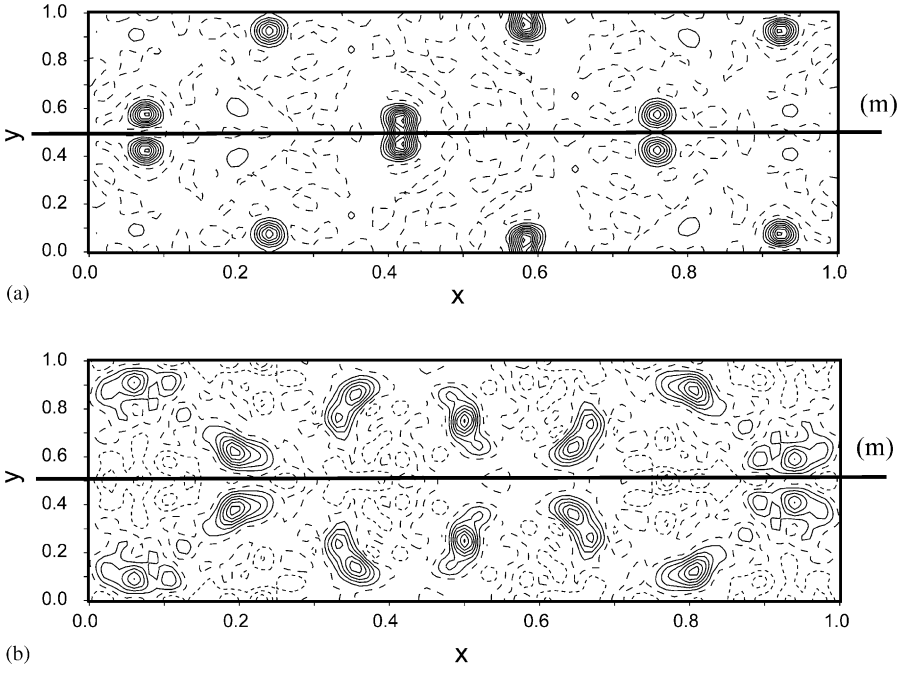

Fig. 3. (a) Observed Fourier maps corresponding to $z = 0.47$ showing the Fe split sites (contour levels $20\,e^-/Å^3$). (b) Fourier difference maps corresponding to $0.46 < y < 0.5$ showing the O split atomic sites (contour levels $2.5\,e^-/Å^3$). The *m* mirror plane responsible for the splitting is shown.

Table 2
Refined structural parameters

Atom	x	y	z	U_{iso} or U_{eq}	Occ.
$Fe_A(1)$	0.4146(13)	−0.5	0.3265(2)	0.0065(11)	
$Fe_A(2)$	0.7515(10)	−0.5	0.3192(4)	0.0034(15)	
$Fe_A(3)$	1.0830(12)	−0.5	0.3169(2)	0.0107(13)	
$O_e(1)$	0	−0.25	0.3190(5)	0.000(2)	
$O_e(2)$	0.5	−0.25	0.3369(6)	0.005(3)	
$O_e(3)$	0.3307(9)	−0.743(4)	0.3262(4)	0.013(3)	
$O_e(4)$	0.8308(9)	−0.765(3)	0.3286(4)	0.012(3)	
$O_a(1)$	0.4050(11)	−0.5	0.4087(8)	0.016(5)	
$O_a(2)$	0.757(2)	−0.5	0.407(2)	0.046(13)	
$O_a(3)$	0.077(2)	−0.5	0.4049(8)	0.021(5)	
$O_a(4)$	0.420(2)	−0.5	0.2542(5)	0.010(4)	
$O_a(5)$	0.75	−0.5	0.25	0.027(13)	
Sr2(1)	0.4175(6)	0	0.25253(9)	0.0107(10)	
Sr2(2)	0.75	0	0.25	0.013(2)	
Sr1(1)/Bi1(1)	0.4117(6)	0	0.38512(13)	0.0180(9)	0.63(2)
Sr1(2)/Bi1(2)	0.7568(6)	0	0.3842(3)	0.0267(15)	0.60(3)
Sr1(3)/Bi1(3)	1.0786(6)	0	0.38139(14)	0.0186(8)	0.74(2)
$Fe_B(1)$	0.0748(3)	−0.4240(6)	0.46818(17)	0.0028(8)	0.5
$Fe_B(2)$	0.4177(5)	−0.4500(5)	0.47489(12)	0.0071(7)	0.5
$Fe_B(3)$	0.7592(4)	−0.4190(11)	0.4711(3)	0.0181(17)	0.5
$O_B(1)$	0.1971(10)	−0.604(3)	0.4769(6)	0.007(3)	0.5
$O_B(2)$	0.6510(10)	−0.652(3)	0.4829(7)	0.014(4)	0.5
$O_B(3)$	0.9387(8)	−0.584(2)	0.4715(6)	0.008(3)	0.5
O_{Bs}	0.5	−0.75	0.5	0.018(4)	

cationic positions, which is not the case for the *Bbmb* solution. The gain for the *R* factors seems to be quite artificial and not physically significant.

The observation of the diffuse scattering in the diffraction pattern is also coherent with the likely existence of this disorder, which results in the apparent mirror plane orthogonal to **b**. This point will be discussed further, but this statistical disorder also supports a refinement in a centrosymmetric symmetry, even if it is clear that local arrangements are probably acentric.

5. Relationships between two 2212s: $Bi_2(Sr_2)SrFe_2O_{9\pm\delta}$ and $Fe_2(Bi_{0.69}Sr_{1.31})SrFe_2O_{9.5\pm\delta/2}$

Highlighting and analysing the structural relationships of the title compound $Bi_{4/3}Sr_{14/3}Fe_8O_{19\pm\delta}$ and $Sr_4Fe_6O_{13\pm\delta}$ with the 2212- and 2201-type phases [21] need to adopt another harmonized formulation.

$Bi_{4/3}Sr_{14/3}Fe_8O_{19\pm\delta}$ exhibits one double perovskite slice $[Sr_2Fe_2O_6]_\infty$ and one complex RS-related $[(Bi,Sr)Fe_2O_{3.5\pm\delta/2}]_\infty$ slice, and $Sr_4Fe_6O_{13\pm\delta}$ one single perovskite slice $[SrFeO_3]_\infty$ and one complex RS-related $[SrFe_2O_{3.5\pm\delta/2}]_\infty$ slice. The 2212-type structure $Bi_2Sr_2SrFe_2O_{9+\delta}$ exhibits one double perovskite slice $[Sr_2Fe_2O_6]_\infty$ and one complex RS-related $[SrBi_2O_{3+\delta}]_\infty$ slice whereas the 2201-type $Bi_2Sr_2FeO_{6+\delta}$ is built up from one single perovskite slice $[SrFeO_3]_\infty$ and one complex RS-related $[SrBi_2O_{3+\delta}]_\infty$ slice. According to the similar building mechanism, $Bi_{4/3}Sr_{14/3}Fe_8O_{19\pm\delta}$ and $Sr_4Fe_6O_{13\pm\delta}$ are two new members of the 2212s and 2201s and can be written $Fe_2(Bi_{0.69}Sr_{1.31})SrFe_2O_{9.5\pm\delta/2}$ and $Fe_2(Sr_2)FeO_{6.5\pm\delta/2}$, respectively. The difference in the oxygen stoichiometry notation is related to the oxidation state of the transition element and to the corresponding ideal chemical formulation. Nevertheless, the different studies have shown an oxygen content close to 6.5 for $Fe_2(Sr_2)FeO_{6.5\pm\delta/2}$ or to 9.5 for $Fe_2(Bi_{0.69}Sr_{2.31})Fe_2O_{9.5\pm\delta/2}$, but which can be increased or decreased depending on the oxydo-reduction process, and this justifies the $\delta/2$ adjustment in the formula.

Large analogies can be found between the present Fe-2212s ferrites and the Bi-2212s cuprates, ferrites and cobaltites [19,28–34]. As a matter of fact, in both types of phases, the RS-type slabs are highly distorted. The previous Bi-2212 structures were refined as incommensurate modulated structures, with significant displacement modulation parameters, both along the stacking direction $\vec{c}$ and along the modulation direction $\vec{a}$. The first ones are responsible for an undulation of the different layers building the slabs. The second ones allow an accommodation between the cationic and oxygen lattices in the RS-type slab, enabling a non-stoichiometry in oxygen and a lattice mismatch between the two types of slabs.

The same types of phenomena can be seen in the present structure. We observe a clear analogy between the present double perovskite slab and the equivalent one in the Bi-2212 structure [27,32], $Bi_{2+x}Sr_{3-x}Fe_2O_{9+\delta}$ (Fig. 4). The modulated displacements along the stacking direction are smaller in the present case, probably in relation with the fact that very closed Fe-RS layers here replace the two independent Bi-RS layers of the previous structure. This difference also explains the lower value of the stacking parameter. The atomic occupancy of the $[FeO]_\infty$ (Fe-RS)

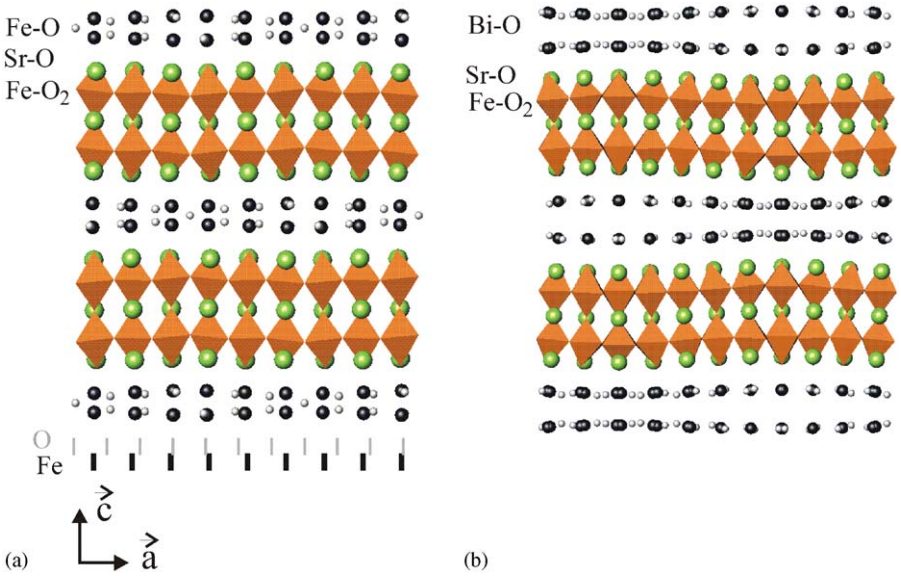

Fig. 4. (a) Schematical representation of the structure projected along **b**. The average periodicity of the Fe and O atoms in the rock salt-type layers is shown. (b) Schematical projection of the $Bi_{2+x}Sr_{3-x}Fe_2O_{9+\delta}$ structure (Perez, PRB).

layer exhibits a fundamental difference with that of the adjacent $[SrO]_\infty$. Owing to the larger displacement of the oxygen atoms along $\vec{a}$, one extra oxygen O_{BS} is periodically inserted for 6 Fe atoms between the two $[FeO]_\infty$ layers. Consequently the oxygen stoichiometry is equal to 7/6 in this layer, against 1 in the $[SrO]_\infty$ layer. The corresponding average Fe and O periodicities in the modulation direction are indicated in Fig. 4a. These different averaged periodicities have been interpreted with a specific second independent O sub-lattice in Bi-based compounds [35,36]. In comparison with the Fe2212 structure, this supplementary oxygen is now a common bridging oxygen between the two layers of the slab, so that the two layers are not completely independent.

The double perovskite layers are very similar to the related ones in $Bi_{2+x}Sr_{3-x}Fe_2O_{9+\delta}$ [27,32] with smaller distortions. The corresponding FeO_6 octahedra present 5 equivalent Fe–O distances around 1.95 Å, but a larger apical Fe–O distance between 2.22 and 2.38 Å. The corresponding bond valences [37,38] are 3.2, 3.1 and 3.2. The mixed Bi–Sr sites, mainly occupied by Sr, are characterized by larger ADP parameters, which are probably related to this occupational disorder.

Both structures also present another common character: the layers of the distorted slab B are disordered. In the case of the Bi-2212 [27] structure, one observed a splitting along the modulation direction, clearly visible in Fig. 4b. It is now replaced by a splitting in the orthogonal direction, not visible in Fig. 4a. Considering the inter-atomic distances between the different disordered atomic sites, the simultaneous occupation of the sites is locally not possible because of too short bonds (Fe–Fe, Fe–O or O–O distances). Different local configurations have been tested; some of them must be ruled out for geometric reasons. Only two configurations result in satisfactory inter-atomic distances and cationic environments. They lead to local crystal symmetries *Bb2b* or *B2/b* (unique axis *c*). In these two configurations, iron and oxygen of the RS-type slabs occupy sites located on the same side of the pseudomirror plane ($y = 0$).

Even if the first *Bb2b* hypothesis cannot be definitively ruled out from our previous criteria, clear analogies with related structures allow us to choose the *B2/b* solution. As a matter of fact, looking at the projection along *c* of the corresponding structural arrangement of an isolated $[FeO]_\infty$ layer in the RS-type block (Fig. 5), and comparing it with the related $[BiO]_\infty$ layer in the Bi-2212 structure, or with the related $[FeO]_\infty$ layer of the $Sr_4Fe_6O_{13\pm\delta}$ [19], the same double A–O chains can be seen, allowing the periodic (commensurate or incommensurate) insertion of the supplementary oxygen atom. The main difference with the so-called Bi-2201 or Bi-2212 structures is the replacement of Bi by Fe. The stereoactivity of the electronic lone pair of Bi^{3+} was responsible for the particular stacking of the corresponding double $[Bi_2O_2]_\infty$ layers [39]. Each individual $[BiO]_\infty$ layer is built from the juxtaposition of double chains, which are directly facing the similar one in the adjacent layer. In the present case, the double Fe–O chains in the adjacent layer are now translated by $b/2$. This implies a smaller thickness of the double $[Fe_2O_2]_\infty$ layers and a smaller *c* parameter [19].

Near the bridging O_{Bs} oxygen atom, the $Fe_B(2)$ coordination can be described by a trigonal bi-pyramid (TBP) with the base defined by the three shorter $Fe_B(2)$–O distances, roughly orthogonal to the $(\mathbf{a_0} + \mathbf{b_0})$ direction, and pointing alternatively along **c** or $-$**c** (Figs. 6–8). A similar environment is also found for the $Fe_B(1)$ atom, but with a different orientation of the basal plane of the bi-pyramid, orthogonal to the modulation direction **a** and pointing alternatively along **b** or $-$**b** (Fig. 7). This last environment

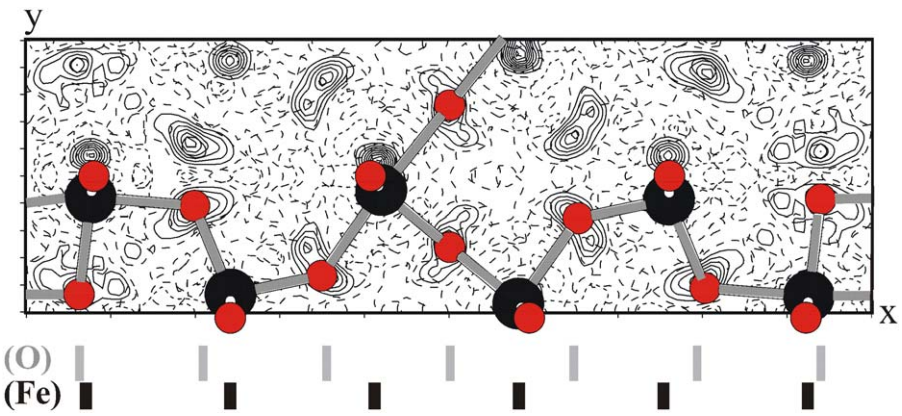

Fig. 5. Superimposed observed Fe and difference O Fourier maps around $y = 0.47$, showing the choice of the atomic Fe (large circles) and O (small circles) atomic sites for the local configurations of the rock salt-type Fe–O layers. The average periodicity of the Fe and O atoms is shown (see Fig. 4).

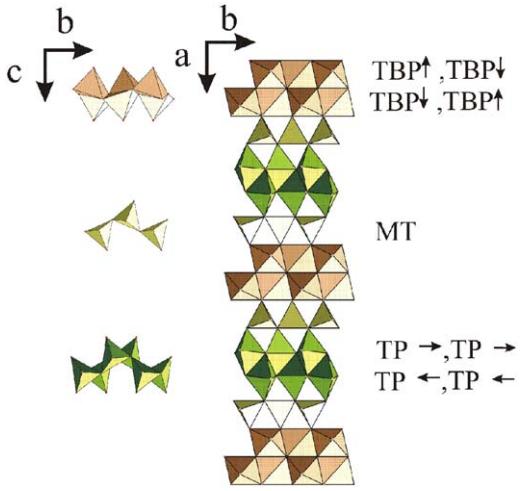

Fig. 6. Schematic representation of the $[(Sr, Bi)_2Fe_4O_{7-\delta}]$ slab (slab B) projected along **b** and along **a**, showing the alternation of trigonal bipyramids (TBP), monocaped tetrahedra (MT) and tetragonal pyramids (TP).

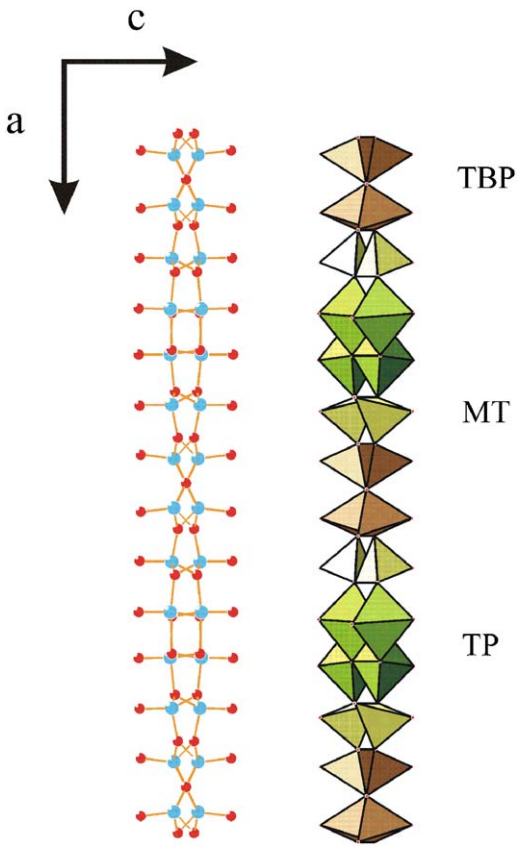

Fig. 7. Schematic representation of the $[(Sr, Bi)_2Fe_4O_{7-\delta}]$ slab (slab B) projected along **b**, showing the alternation of trigonal bipyramids (TBP), monocaped tetrahedra (MT) and tetragonal pyramids (TP).

can also be described by a distorted TP, with the base in the (**a**, **c**) plane, similar to the TPs of the $Sr_4Fe_6O_{13\pm\delta}$ structure [19]. Between these two pyramids, the $Fe_B(3)$ atom is at the centre of a tetrahedron (Fe–O distances between 1.79 and 1.90 Å and O–Fe–O angles between 99° and 126°) (monocaped tetrahedron MT, according the same terminology as in [20]), the next neighbour oxygen atom is at around 3 Å. A bond valence calculation [37,38] for these different sites leads to values of 2.9, 3.1 and 3.1, respectively. The corresponding distorted RS-type slab is schematically represented in Figs. 6 and 7; it shows large similarities with the related slab of the $Sr_4Fe_6O_{13\pm\delta}$ structure. The main difference is related to the different value of the modulation vector (1/3 in the present case), which is realized here by the regular alternation of one double ribbon of TBPs [TBP↑][TBP↓] and a ribbon of mixed polyhedra [MT][TP][TP][MT].

The bridging oxygen site O_{Bs} can also be the key to propose a structural hypothesis concerning the partial structural disorder revealed by the diffuse scattering lines along **c***. As a matter of fact, it can be considered as a hinge: on both sides of this site, one can easily imagine that the two local possible disordered configurations related by the mirror plane m_z are equiprobable, and the corresponding structural assumptions are schematically shown in Fig. 9. When considering only a completely disordered structure with a partial half-occupation of all the disordered sites, the modulated period corresponds to $3\mathbf{a_0}$

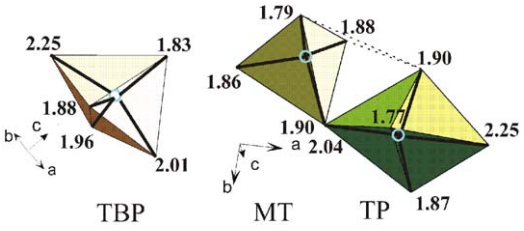

Fig. 8. Schematic representation of the different Fe environments in the $[(Sr, Bi)_2Fe_4O_{7-\delta}]$ slab (slab B) and corresponding Fe–O distances.

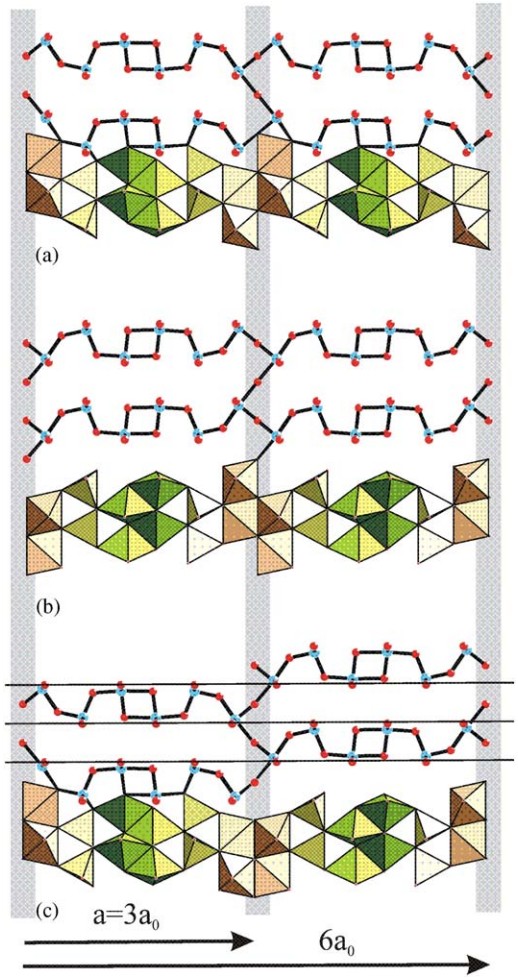

Fig. 9. Schematic representation of the assumed disordered configuration of the $[(Sr, Bi)_2Fe_4O_{7-\delta}]$ slab (slab B): (a) First non-disordered structural hypothesis in $B2/b$ symmetry. (b) Corresponding symmetry related configuration through the mirror plane m_y. (c) Alternation of the two configurations with the corresponding doubled periodicity related to the diffuse scattered lines.

(the distance between two successive O_{Bs} site in a double Fe–O chain). Considering now a regular alternation of the two possible local configurations on both sides of each O_{Bs} site, a double periodicity $6\mathbf{a_0}$ characterizes this structural model (Fig. 9b). One can easily imagine such a planar local ordering in the (**a**, **b**) plane with no correlation in the stacking **c** direction. This structural assumption could explain the diffuse lines along **c***, which are characterized by a modulation vector $5/6\mathbf{a_0}^*$, or $1/6\mathbf{a_0}^* + \mathbf{c}^*$. Then they should be compatible with a super-space symmetry $Fmmm(\alpha',0,1)$, compatible with the previous double periodicity. Such partial planar ordering of two equiprobable local configurations, resulting in diffuse scattering lines, are encountered in $Sr_4Fe_6O_{13\pm\delta}$ [19].

6. ^{57}Fe Mössbauer study of $Fe_2(Bi_{0.69}Sr_{1.31})SrFe_2O_{9.5\pm\delta/2)}$

The Mössbauer study was carried out on the powder sample. The EDS analysis of more than thirty crystallites showed that the actual cationic compound is very close to the nominal one and the chemical titration confirmed the trivalent oxidation state of iron (in the limit of the technique accuracy). The ED analyses showed a statistical distribution of $q = \alpha a^* + c^*$, with $0.33 < \alpha < 0.37$, suggesting that the powder sample is slightly more oxidized than the single crystal.

The Mössbauer spectrum of this compound recorded at 80 K (Fig. 10) shows that all iron ions are magnetic at this temperature. The best fit was obtained with four Mössbauer components, their hyperfine parameters are given in Table 3. The observed isomer shift values ($0.33 \leqslant IS \leqslant 0.44$ mm/s) are typical for iron ions in the trivalent state. From *A* to *D* sites, the hyperfine field (H_f) value decreases from 53.9 to 40.5 T, while the quadrupole shift (2ε) one increases from −0.36 to 0.90 mm/s, respectively. This fact is due to the difference between the local environments of these four Mössbauer sites.

In order to correctly attribute these components to different types of Fe environment evidenced by the above structural study, we have considered the value of H_f in each

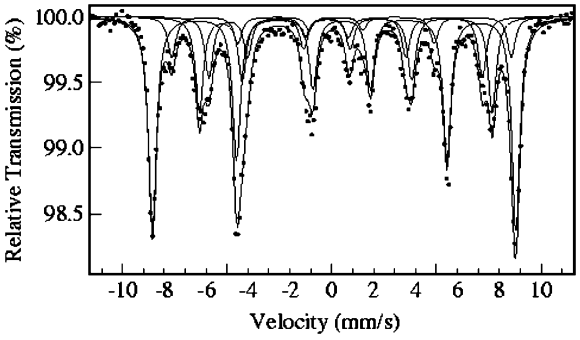

Fig. 10. Mössbauer spectrum recorded for the powder sample.

Table 3
Fitted ^{57}Fe hyperfine Mössbauer parameters, at 80 K, of the $Bi_4Sr_{14}Fe_{24}O_{56}$ compound

IS ± 0.01 (mm/s)	2ε ± 0.01 (mm/s)	H_f ± 0.1 (T)	% ± 2	Attributed Fe^{3+} environment
0.41	−0.36	53.9	50	A octahedral
0.44	0.27	50.4	12	B pyramidal
0.33	0.90	43.4	21	C bipyramidal
0.33	0.90	40.5	17	D tetrahedral

case. First, the component A with highest H_f value (53.9 T) corresponds clearly to Fe^{3+} in octahedral site, its ratio (50%) agrees also with structural results. If we assume that, as a general rule, the pyramidal environment is more symmetric than the bi-pyramidal one and the same way between the bi-pyramid and the tetrahedron, then the corresponding H_f value should be decreased when the site symmetry decreases. With this consideration and taking into account the structural results and the observed H_f values of this compound, we can now attribute the *B*, *C* and *D* sites to the pyramidal, bi-pyramidal and tetrahedral Fe^{3+} environments, respectively (Table 3). As well, we have effectively observed that the 2ε and H_f values of the *B* site are, respectively, smaller and larger than the values of the *C* and *D* components. Furthermore, the *B*, *C* and *D* fitted Mössbauer ratios are closed to that obtained by structural analyses results for the case $\alpha = 0.35$, in which the pyramidal, bi-pyramidal and tetrahedral site ratios are estimated equal to 12%, 21% and 17%, respectively.

7. Structural mechanism of the new family

Coming back to the 2201s member $Fe_2(Sr)_2FeO_{6.5\pm\delta/2}$, the $[Fe_2O_{2.5\pm1/2\delta}]_\infty$ double layer made of TPs, MTs and TBPs FeO_5, exhibiting commensurate or incommensurate modulations depending on the oxygen non-stoichiometry (Fig. 11). Starting from commensurate structures $\delta = 0$ and $\alpha = 0.5$, $Sr_4Fe_6O_{13}$, the sequence is ([TP][TP])([TBP↑][TBP↓]), made of double blocks of TPs alternating with TBPs. As δ increases, α decreases and triple blocks replace, in an ordered way or not, the double TPs. The triple blocks are built up from one TP sandwiched between two MTs ([MT][TP][MT]). The complete replacement correspond to a commensurate structure with the sequence ([TBP↑][TBP↓])([MT][TP][MT]) involving $\delta = 0.2$, $\alpha = 0.4$ and the stoichiometry $Sr_4Fe_6O_{12.8}$.

From the HREM images of the title compound, it was observed that the extension of the structural mechanism over a larger extent, $\delta > 0.2$, would involve a block of four polyhedra, retaining unchanged the ([TBP↑][TBP↓]) double block. That means that the insertion of a quadruple block is associated to the increase of δ. According to that construction mode, the limit of the sequence is ([TBP↑][TBP↓])([MT][TP][TP][MT]), with $\alpha = 1/3$, which that of the present compound. As previously reported [20], the intergrowth sequence between $[(Bi,Sr)Fe_2O_{3.5\pm1/2\delta}]_\infty$ RS-type layers and double perovskite layers is easily interpretable in the HREM images. This is illustrated in Fig. 12 (focus value close to −575 Å), where the zones of high electron density are imaged as brighter spots. The three rows of brighter dots (spaced by about 2.9 Å along *a*) are correlated to the superposition of the Sr and O atoms, whereas as the greyer dots are correlated to iron positions. The theoretical HREM images have been calculated, using the positional parameters given in Table 2 and superimposed with the experimental one in Fig. 12. This is a classical working mode for layered materials.

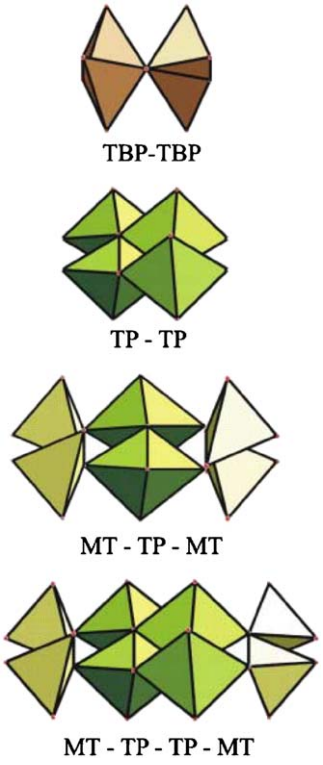

Fig. 11. Schematical drawing of the different blocks sandwiched between the ([TBP↑][TBP↓]) double blocks and varying with α.

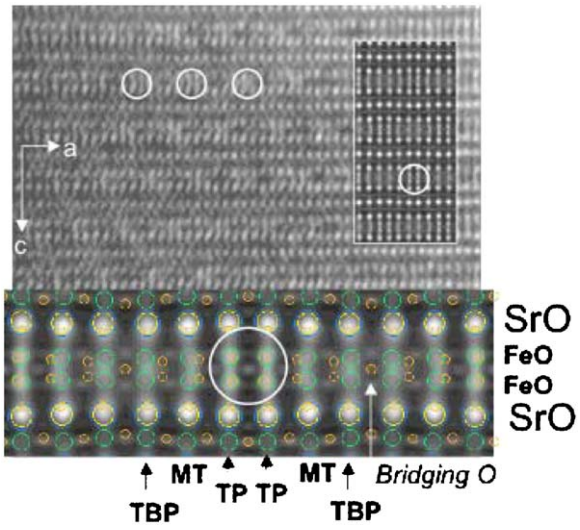

Fig. 12. [010] HREM recorded for a focus close to −575 Å and enlargement of the calculated image and projected potential.

In the present compounds, the important point deals with the interpretation in terms of iron polyhedra from the experimental contrast at the level of the $[Fe_2O_{2.5\pm1/2\delta}]_\infty$ double layer. Certain focus values of the HREM images are sensitive to small displacements of oxygen atoms but a direct interpretation is not straightforward. In Fig. 12, the characteristic contrast of this focus value at the level of the iron double layer is the formation of double brighter sticks (parallel to $\vec{c}$), typical of the iron atoms in TP environment.

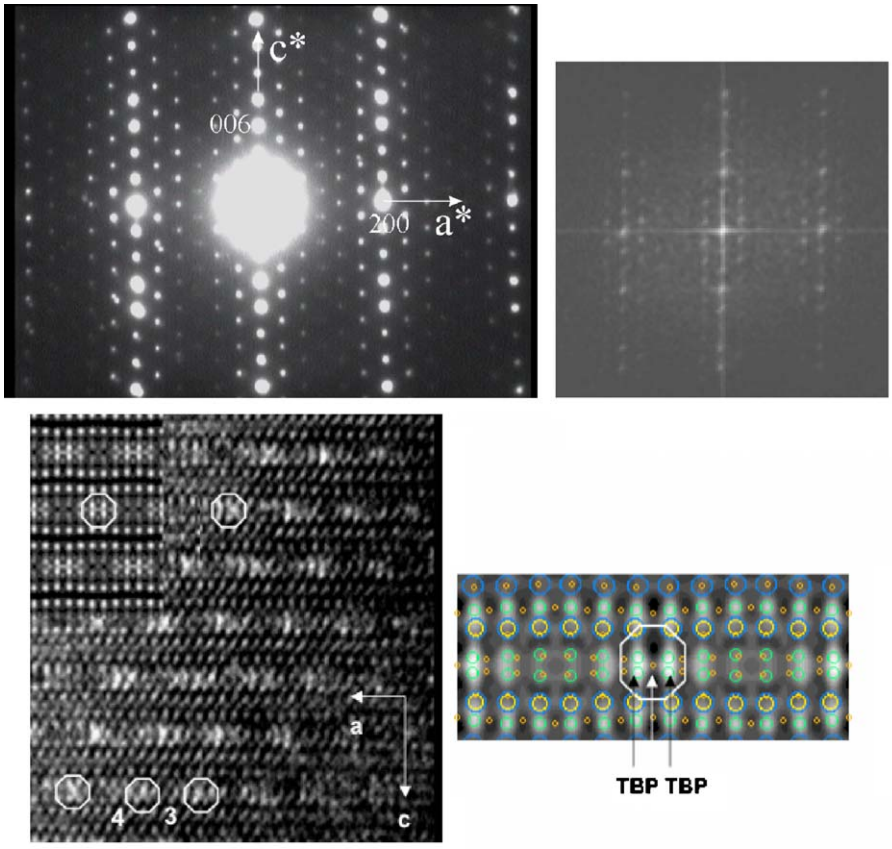

Fig. 13. (a) [010] ED pattern ($\alpha \approx 0.35$), (b) FFT and (c) [001] HREM experimental image recorded for a focus value close to 50 Å illustrating the origin of the incommensurate modulation. The enlarged calculated image and projected potential are given.

The simulation shows that the brighter contrast is generated by the positions of the surrounding oxygen atoms which are exactly projected over the iron positions, contrary to the Fe and O atoms of the MTs and TBPs. Another interesting contrast is observed in the thicker part of the crystals, for a focus value close to 50 Å, with white crossed double spots at the level of the $[Fe_2O_{2.5\pm1/2\delta}]_\infty$ double layers. These crossed-like double spots are associated to the [TBP↑][TBP↓] blocks (circled by white octogones in Fig. 13c) and separated along $\vec{a}$ by three or four grey double spots (two periodicities are white numbered). This evidenced the existence of blocks of three ([MT][TP][MT]) and four ([MT][TP][TP][MT]) blocks, in agreement with the experimental ED pattern (Fig. 13a) and the FFT (Fig. 13b), which show that the α value is incommensurate. Investigating numerous crystallites, no single double block [TP][TP] is inserted between the [TBP↑][TBP↓] blocks for the intermediate α values ($0.4 > \alpha > 1/3$), since they likely should involve strong strains in the framework.

Note that for the modulated structure of the oxygen deficient compound $Sr_4Fe_6O_{13-\delta}$, the relationships between the modulation vector and oxygen content is, theoretically, $\vec{q} = \alpha\vec{a}^* + \vec{c}^*$, with $\alpha = (1-\delta)/2$ i.e. $\delta = (1-2\alpha)$. Since the $[Fe_2O_{2.5\pm1/2\delta}]_\infty$ double layer is common to both $Fe_2(Sr_2)FeO_{6.5\pm1/2\delta}$ and $Fe_2(Bi_{0.69}Sr_{1.31})SrFe_2O_{9.5\pm1/2\delta}$ structures, the $\alpha = 1/3$ value implies $\delta = 0.33$, i.e. $Fe_2(Bi_{0.69}Sr_{1.31})SrFe_2O_{9.333}$ for the present compound and, by the way, only trivalent iron, in agreement with the Mössbauer study.

8. Concluding remarks

An accurate description of the structure of $Bi_{4/3}Sr_{14/3}Fe_8O_{19\pm\delta}$, especially the actual nature of the iron environment at the level of the complex $[SrFe_2O_{3.5\pm\delta/2}]_\infty$ slice, has been carried out to the refinement from single crystal X-ray diffraction. The analysis of this structure and that of $Sr_4Fe_6O_{13\pm\delta}$ allows understanding the variation of this environment with the amplitude of the modulation vector. Large structural analogies with the Bi-2201s and Bi-2212s phases have been detailed, leading to a formulation $Fe_2(Sr)_2FeO_{6.5\pm\delta/2}$ and $Fe_2(Bi_{0.69}Sr_{1.31})SrFe_2O_{9.5\pm1/2\delta}$ for these Fe-2201s and Fe-2212s phases, respectively. These observations considerably enlarge the family of the layered structures and open the route to the discovery of new structural mechanisms.

References

[1] B.C.H. Steele, Mater. Sci. Eng. B 13 (1992) 79.
[2] N.Q. Minh, J. Am. Ceram. Soc. 76 (1993) 563.

[3] K.R. Kendall, C. Navas, J.K. Thomas, H.C. Loye, Solid State Ionics 82 (1995) 215.
[4] U. Balachandra, B. Ma, P.S. Maiya, M.S. Kleefish, T.P.
[5] B. Ma, U. Balachandran, J.-H. Park, C.U. Segre, Solid State Ionics 83 (1996) 65.
[6] B. Ma, U. Balachandran, J.-H. Park, J. Electrochem. Soc. 143 (1996) 1736.
[7] B. Ma, U. Balachandran, Solid State Ionics 100 (1997) 53.
[8] S. Kim, Y.L. Yang, R. Christoffersen, A.J. Jacobson, Solid State Ionics 109 (1998) 187.
[9] M.V. Patrakeev, E.B. Mitberg, I.A. Leonidov, V.L. Kozhevnikov, Solid State Ionics 139 (2001) 325.
[10] S. Guggilla, T. Armstrong, A. Manthiram, J. Solid State Chem. 145 (1999) 260.
[11] A. Yoshiasa, K. Ueno, F. Kanamaru, H. Horiuchi, Mater. Res. Bull. 21 (1998) 175.
[12] E. Fjellvag, B.C. Hauback, R. Bredesen, J. Mater. Chem. 7 (12) (1997) 2415.
[13] B.J. Mitchell, J.W. Richardson Jr., C.D. Murphy, B. Ma, U. Balachandran, J.P. Hodges, J.D. Jorgensen, J. Eur. Ceram. Soc. 22 (2002) 661.
[14] J.C. Waerenborgh, M. Avdeev, M.V. Patrakeev, V.V. Kharton, J.R. Frade, Mater. Lett. 57 (2003) 3245.
[15] R. Bredesen, T. Norby, A. Bardal, V. Lynum, Solid State Ionics 135 (2001) 687.
[16] M.D. Rossel, A.M. Abakumov, G. Van Tendeloo, J.A. Pardo, J. Santiso, Chem. Mater. 16 (2004) 2578.
[17] B. Mellenne, R. Retoux, C. Lepoittevin, M. Hervieu, B. Raveau, Chem. Mater. 16 (24) (2004) 5006.
[18] M.D. Rossel, A.M. Abakumov, G. Van Tendeloo, M. Lomakov, S. Ya Istomin, E. Antipov, Chem. Mater. 17 (2005) 4717.
[19] O. Pérez, B. Mellenne, R. Retoux, B. Raveau, M. Hervieu, Solid State Sci. 8 (2006) 431.
[20] C. Lepoittevin, S. Malo, M. Hervieu, D. Grebille, B. Raveau, Chem. Mater. 16 (2004) 5731.
[21] B. Raveau, C. Michel, M. Hervieu, D. Groult, Crystal chemistry of High Tc superconducting copper oxides, in: Springer Series in Materials Science, vol. 15, Springer, Berlin, 1991 331pp.
[22] A. Duisenberg, L. Kroon-Batenburg, A. Shreurs, J. Appl. Crystallogr. 36 (2003) 220.
[23] G.M. Sheldrick, Sadabs program for scaling and correction of area detector data, Göttingen, 1997.
[24] V. Petricek, M. Dusek, L. Palatinus, JANA2000, The Crystallographic Computing System, Institute of Physics, Praha, Czech Republic, 2000.
[25] T. Janssen, A. Janner, A. Looijenga, P.M. de Wolff, International Tables for Crystallography, vol. C, Kluwer, Dordrecht, 1992, p. 797.
[26] P.M. de Wolff, T. Janssen, A. Janner, Acta Crystallogr. A 37 (1981) 625.
[27] O. Pérez, H. Leligny, D. Grebille, J.M. Grenêche, Ph. Labbé, D. Groult, B. Raveau, Phys. Rev. B 55 (1997) 1236.
[28] M. Hervieu, C. Michel, N. Nguyen, R. Retoux, B. Raveau, Eur. J. Solid State Inorg. Chem. 2 (1988) 375.
[29] Y. Lepage, W.R. McKinnon, J.M. Tarascon, P. Barboux, Phys. Rev. B 40 (1989) 6810.
[30] R. Retoux, C. Michel, M. Hervieu, N. Nguyen, B. Raveau, Solid State Commun. 69 (1989) 599.
[31] V. Sedykh, F. Fujita, I. Smirnova, A. Dubovitskii, B. Narymbetov, V. Shekhtman, Jpn. J. Appl. Phys. 34 (1995) 4033.
[32] O. Pérez, H. Leligny, G. Baldinozzi, D. Grebille, M. Hervieu, P. Labbe, D. Groult, H. Graafsma, Phys. Rev. B 56 (1997) 5662.
[33] D. Hechel, I. Felner, Physica B 262 (1999) 410.
[34] N. Jakubowicz, D. Grebille, H. Leligny, M. Evain, J. Phys. Condens. Matter 11 (1999) 3997.
[35] J. Etrillard, P. Bourges, C.T. Lin, Phys. Rev. B 62 (2000) 150.
[36] D. Grebille, H. Leligny, O. Pérez, Phys. Rev. B 64 (2001) 106501.
[37] I.D. Brown, D. Altermatt, Acta Crystallogr. B 41 (1985) 244.
[38] N.E. Brese, M. O'Keefe, Acta Crystallogr. B 47 (1991) 192.
[39] N. Jakubowicz, O. Pérez, D. Grebille, H. Leligny, J. Solid State Chem. 139 (1998) 194.